electronics

MDPI

Article

Three-Dimensional Helicoidal Antennas for Near-Field Communication Wireless Charging in Smart Ring Applications: Design, Modelling, and Comparison to Representative Planar Reference Antennas

Lilian Rolle [1,2,*], Thibaut Deleruyelle [2], Alain Loussert [2] and Jérémy Quignon [1]

[1] STMicroelectronics, 13106 Rousset, France; jeremy.quignon@st.com
[2] IM2NP, Aix Marseille Univ, ISEN-YNCREA Méditerranee, IMNP, 83000 Toulon, France; thibaut.deleruyelle@yncrea.fr (T.D.); alain.loussert@yncrea.fr (A.L.)
* Correspondence: lilian.rolle@st.com

Abstract

The deployment of embedded near-field communication (NFC) wearable devices continues to grow with the Internet of Things (IoT). Constraints on bill of materials (BOM) cost, representing all the components of a device, and available space lead manufacturers to seek alternatives to implement wireless charging. This article introduces an antenna solution to respond to requirements of NFC charging applications for smart ring form factors. The proposed study includes electrical parameter modelling, estimation of inductance, resistance, quality factor, and coupling coefficient together. This 3D helicoidal antenna operates in quasi-magnetostatic mode. The different pairs are then compared to existing representative planar reference antennas in simulation. The results are confirmed with experimental validation for the best case, worst case, and typical case. First, the article presents the different antennas produced. It defines the pairs of antennas and their respective coupling coefficients. The methodology to simulate and measure losses is also presented. Then, the article compares a representative planar reference with a prototype. The proposed methodology is validated through a comparison of simulations performed with identical S-parameters. This comparison demonstrates both the robustness of the model and the end-to-end charging performance of the prototype. Finally, the article presents a comparative simulation at 2 W and 3 W for all prototype pairs. All antennas provide improved end-to-end power transfer performance, achieving simulated efficiencies up to 64.2%, representing a maximum absolute improvement of 26.2 percentage points, with an average absolute improvement of 22 percentage points in the end-to-end efficiency compared to pre-existing representative planar reference antennas at the same operating power.

Keywords: NFC; NFC WLC; NFC charging; 13.56 MHz; antenna; antenna coupling; power transfer; wireless charging; end-to-end

Check for updates

Academic Editor: Jiangtao Huangfu

Received: 6 August 2026
Revised: 4 September 2026
Accepted: 15 September 2026
Published: 20 September 2026

Copyright: © 2026 by the authors. Licensee MDPI, Basel, Switzerland. This article is an open access article distributed under the terms and conditions of the Creative Commons Attribution (CC BY) license.

1. Introduction

NFC technology is widely adopted in IoT and medical applications. The NFC Forum standard continuously evolves, with the 2021 version introducing NFC Forum Wireless Charging (NFC Forum WLC). Manufacturers increasingly integrate NFC into compact wearable devices such as smartwatches, fitness bands, and smart rings (such as Samsung's

Galaxy Ring [1]). These devices enable continuous health monitoring and facilitate services like public transportation access. A key industrial challenge is waterproofing these devices for everyday use. Additionally, miniaturization imposes strict dimension constraints. Smart rings exemplify this trend and are particularly popular in the Asian market [2]. Achieving waterproofing within extremely limited space while maintaining compliance with NFC standards presents significant engineering challenges. The target market also determines product quality criteria. Another important challenge for wearable devices is to include wireless charging in small devices. Many of these connected devices already have NFC. The challenge is to implement wireless charging without increasing the BOM [3]. The coexistence and interoperability of wireless power transfer and NFC systems are critical, as investigated in [4]. For medical applications, the ability to deliver wireless power to a device with high efficiency and therefore enable battery-free operation is important for future applications such as active implantable devices [5] or optogenetic implants with highly constrained receiver volumes [6]. According to main market products, antenna shapes are 2D, either circular, square, or rectangular, as developed in [7], indicated in [8–10] or proposed as a dual-antenna flexible system in [11]. While commercial smart rings rely on dedicated chargers, academic works have explored seamless charging alternatives. For instance, ref. [12] proposed a wireless power transfer system to power a smart health tracking ring using a smartphone's reverse wireless charging feature.

This paper proposes a complete analytical and experimental methodology for the design, modelling, and validation of concentric 3D helicoidal NFC antennas dedicated to smart ring wireless charging. The proposed approach enables antenna performance to be predicted before fabrication and demonstrates significant improvements in end-to-end wireless power transfer compared to representative commercial planar antennas.

The core novelty of the proposed work lies in applying 3D helicoidal antenna geometry to the highly constrained area of wearable wireless charging. Such geometries are usually not used in these applications. Specifically, this paper implements an analytical modelling framework compiled from classic electromagnetic formulations and validates it using experimental prototypes wound on 3D-printed supports. Table 1 below summarizes the main characteristics of the state of the art and of the work proposed.

Table 1. A comparison of the characteristics of the state of art against the proposed work.

Reference	Frequency	Antenna Geometry	Antenna Size	End-to-End Efficiency (%)	Application
[5]	13.56 MHz	Planar circular	Ø = 39 mm	56.50% Measured	Medical implant
[6]	7.15 MHz	Planar rectangle	6 × 11.25 mm	4.10% Measured	Optogenetic implant
[12]	170.07 kHz	Curved planar rectangle	10 × 60 mm	13.39% Measured	Smart ring
Planar reference	13.56 MHz	Planar rectangular	20.3 × 5.3 mm	41.40% Simulated	Small wearable
Proposed work	13.56 MHz	3D helicoidal	Ø = 21.5 H = 5 mm	57.00% Measured	Smart ring

Furthermore, a rigorous end-to-end power transfer efficiency comparison is conducted, evaluating the proposed 3D helicoidal prototypes against representative planar reference antennas.

2. Materials and Methods

2.1. Mechanical Constraints and Antenna Dimensions

The specific wearable device considered in this study is the smart ring. These devices are experiencing significant growth in the Asian and North American markets, as shown in [2]. This application fundamentally constrains and defines the antenna dimensions. In the United States, the most common ring size for women is 7.0 [13]. This size has an inner diameter of 17.3 mm. However, the average ring size for men is 11 [13]. This size corresponds to an inner

diameter of 20.6 mm. On average, smart rings feature a thickness of approximately 2.6 mm and a total height of approximately 7.5 mm, as indicated in Table 2 below.

Table 2. Dimensions of market smart rings according to references [14–23].

Smart Ring Name	Height	Thickness	Reference
Evie Ring	8.00	3.00	[14]
Amazfit Helio Ring	8.00	2.60	[15]
Noise Luna Ring	8.00	2.90	[16]
Soxai Ring	6.70	2.70	[17]
Velia Ring	5.20	2.50	[18]
Oura ring 4	7.90	2.88	[19]
Circular pro	7.80	2.55	[20]
RingConn	8.10	2.30	[21]
Ultrahuman ring Air	8.10	2.60	[22]
Samsung galaxy ring	7.00	2.60	[23]
Average	7.48	2.66	X

Considering the constraints imposed by the external casing, a 2 mm clearance is allocated between the inner diameter of the ring and the antenna. In terms of antenna height, a 1 mm clearance is considered at both the top and bottom edges of the 7.5 mm average ring height. This results in an available antenna height of 5.5 mm. To simplify fabrication, this value is rounded to 5 mm. Based on these constraints, the theoretical receiver antenna diameters range from 19.3 mm to 22.6 mm. These dimensions are standardized to 19.5 mm and 22.5 mm for the sake of manufacturing. A third, intermediate receiver antenna is also designed with a diameter of 21.5 mm. These three antennas share a common height of 5 mm.

Concerning the emitter antenna, which is integrated into the ring charging or polling enclosure, two configurations are evaluated: one in which the emitter is positioned around the ring and another in which the emitter is positioned inside the inner surface of the ring. The medium-sized receiver makes it possible to assess the effect of the radius mismatch on the coupling coefficient. By using only two emitters, both configurations can be evaluated under best-case, worst-case, and intermediate distance conditions.

Maintaining a 2 mm mechanical clearance for the casing sets the maximum outside limit and the minimum inside limit. These limits correspond to emitter antenna diameters of 26.5 mm and 15.5 mm, respectively. The emitter axial length must be sufficient to provide a uniform magnetic field over the entire coupling region. This length must correspond to the 5 mm axial length of the receiver antenna. According to [24], when a solenoid emitter is centred at the origin of an orthogonal coordinate system, the generated magnetic field remains highly uniform in the central region. This region is equivalent to half of the length of the antenna. Based on this criterion, an emitter length of 10 mm is selected for the 5 mm long receiver antennas.

The antenna geometries were therefore selected according to the dimensional constraints of the targeted smart ring application. The chosen geometries are summarized in Table 3 below and are then evaluated using the electromagnetic models described in Section 2.2 below.

The objective was not to perform global geometrical optimization, but to identify suitable antenna pair configurations within the available integration volume.

Table 3. Dimensions of antennas based on average ring sizes indicated in [2].

Antenna	Diameter (mm)	Height (mm)
Large emitter	26.5	10
Small emitter	15.5	10
Large receiver	22.5	5
Medium receiver	21.5	5
Small receiver	19.5	5

2.2. Modelling of the Antenna's Characteristics

Once the antenna geometries have been determined from the mechanical constraints presented in the previous section, their electrical characteristics are analytically predicted before prototype fabrication. The proposed methodology successively estimates the self-inductance, AC resistance, quality factor, and magnetic coupling of each antenna pair.

The structural and electromagnetic characteristics of these antennas are calculated with Equations (1)–(27). All distance units are meters (m), all inductance units are Henry (H), and all resistances are in Ohm (Ω):

$$L_s = \frac{4\pi^2 a^2 N^2}{b} K_N \tag{1}$$

where a is the coil radius, b is the axial length, N is the number of turns, and K_N represents the Nagaoka [25] correction factor calculated as follows:

$$K_N = \frac{1}{3\pi\sqrt{(q_1)(1+\alpha_1)^2}}\left[1 - \frac{{k_N}'^2}{{k_N}^2} + \frac{\left\{\frac{{k_N}'^2}{{k_N}^2}\left(1 + \frac{8\beta_1}{1+\alpha_1}\right) + \frac{8\gamma_1}{1-\delta_1}\right\}}{2} log_e\left(\frac{1}{q_1}\right)\right] - \frac{4}{3\pi}\frac{k_N}{k_N\prime} \tag{2}$$

The series expansions define the secondary parameters:

$$\alpha_1 = {q_1}^2 + {q_1}^6 + {q_1}^{12}, \tag{3}$$

$$\beta_1 = {q_1}^2 + 3{q_1}^6 + 6{q_1}^{18}, \tag{4}$$

$$\gamma_1 = q_1 - 4{q_1}^4 + 9{q_1}^9, \tag{5}$$

$$\delta_1 = 2q_1 - 2{q_1}^4 + 2{q_1}^9. \tag{6}$$

The Jacobi theta functions depend on the parameter q_1:

$$q_1 = \frac{l_1}{2} + 2\left(\frac{l_1}{2}\right)^5 + 15\left(\frac{l_1}{2}\right)^9, \tag{7}$$

$$l_1 = \frac{1-\sqrt{k_N}}{1+\sqrt{k_N}} = \frac{{k_N}'^2}{(1+k_N)\left(1+\sqrt{k_N}\right)^2}. \tag{8}$$

where the geometric moduli are given as follows:

$${k_N}^2 = \frac{4a^2}{4a^2+b^2}, \tag{9}$$

$${k_N}'^2 = \frac{b^2}{4a^2+b^2}, \tag{10}$$

$$k_N = \sqrt{{k_N}^2}, \tag{11}$$

$$k_N\prime = \sqrt{{k_N}'^2}. \tag{12}$$

Truncating these equations to three terms provides sufficient accuracy for this application.

Alternatively, for quick verification, the Wheeler formula given in [26] adapted to SI units can be utilized. Since the core consists of air, the magnetic permeability simplifies to μ_0:

$$L_s = \frac{\mu_0 \pi N^2 r^2}{h + 0.45d}. \tag{13}$$

The total resistance R_s is modelled by considering both skin and proximity effects. As demonstrated in the literature, the classic Butterworth–Medhurst equations shift drastically when the length-to-diameter ratio drops below $\frac{l}{D} < 0.2$, requiring empirical correction factors. However, this extreme flat geometry does not apply to our single strand, multiturn 3D coils. The total resistance [27] is expressed as follows:

$$R_s = R_{AC}\phi. \tag{14}$$

where R_{AC} is the standard high-frequency resistance including Rayleigh's skin depth (δ):

$$R_{AC} = \frac{\rho l_{wire}}{\pi_{wire}\delta}, \tag{15}$$

$$\delta = \sqrt{\frac{\rho}{\pi f \mu}}, \tag{16}$$

$$l_{wire} = N\sqrt{(\pi D)^2 + p^2}. \tag{17}$$

The proximity factor ϕ accounts for interturn magnetic constriction and depends on the pitch diameter ratio x and the proximity effect of Medhurst α_p:

$$\phi = 1 + \alpha_p x^2, \tag{18}$$

$$x = \frac{wire}{p}. \tag{19}$$

With the self-inductance equations, Equations (1) or (13), and the resistance of the antennas from Equation (14), we can calculate the quality factor of the antennas using Equation (20) below from [28]. The frequency used is the NFC application frequency: 13.56 MHz.

$$Q = \frac{2\pi f L_s}{R_s}. \tag{20}$$

The antenna shapes proposed in this work require significant modifications compared to the efficiency of the usual planar reference antennas studied in [29]. At this point, the calculations of mutual inductance and coupling coefficient are similar for various antenna shapes:

From the self-inductances of Equations (1) and (13), the mutual inductance M_{12} and coupling coefficient k of the concentric solenoids can be estimated. When the emitter radius is strictly smaller than the receiver radius, a direct flux geometric approximation is used:

$$M_{12} = \frac{\mu_0 \, \pi \, {r_{emitter}}^2 \, N_{emitter} \left(\frac{l_{receiver}}{l_{emitter}}\right) N_{receiver}}{\sqrt{{r_{receiver}}^2 + \left(\frac{l_{receiver}}{2}\right)^2}}. \tag{21}$$

In this formulation, $\mu_0 \cdot \pi \cdot {r_{emitter}}^2$ represents the peak magnetic flux per unit length generated by the primary. The term $N_{emitter}\left(\frac{l_{receiver}}{l_{emitter}}\right)$ estimates the effective primary turns overlapping the receiver length, while $N_{receiver}$ scales the total linkage to the number of turns

of the receiver. The denominator $\sqrt{{r_{receiver}}^2 + \left(\frac{l_{receiver}}{2}\right)^2}$ acts as a geometric attenuation factor toward the receiver centre.

However, this approximation diverges when the emitter radius becomes comparable to or larger than its length. In such very short coil configurations, end flux leakage dominates, requiring a full elliptic integration. This integration is based on the Maxwell–Neumann filament method, adjusted by Rosa and Grover [25], used by Grover works [30] and indicated in Conway's work [31]:

$$M_{12} = \frac{(\mu_0 N_{emitter} N_{receiver})}{(l_{emitter} l_{receiver})} \int_{-\frac{l_{emitter}}{2}}^{\frac{l_{emitter}}{2}} \int_{-\frac{l_{receiver}}{2}}^{\frac{l_{receiver}}{2}} M_{Maxwell}(r_{emitter}, r_{receiver}, z_{emitter} - z_{receiver}) dz_{receiver} dz_{emitter}, \quad (22)$$

$$M_{Maxwell} = \mu_0 \sqrt{r_{emitter} r_{receiver}} \left(\left(\frac{2}{y} - y\right) K(y) - \left(\frac{2}{y}\right) E(y) \right), \quad (23)$$

$$y = \sqrt{\frac{(4\, r_{emitter} r_{receiver})}{\left((\, r_{emitter} + r_{receiver})^2 + (z_{emitter} - z_{receiver})^2 \right)}}. \quad (24)$$

where $K(y)$ and $E(y)$ are the complete elliptic integrals of the first and second kind:

$$K(y) = \int_0^{\frac{\pi}{2}} \frac{1}{\sqrt{1 - y^2 \sin^2 \theta}} d_\theta, \quad (25)$$

$$E(y) = \int_0^{\frac{\pi}{2}} \sqrt{1 - y^2 sin^2 \theta} d_\theta. \quad (26)$$

Finally, we can calculate the coupling coefficient k:

$$k = \frac{M_{12}}{\sqrt{L_{emitter} L_{receiver}}} \quad (27)$$

From Equations (1), (13), (14) and (20), we can complete Table 4 with the dimensions of the antennas determined in Section 2.1:

Table 4. Modelled inductance and resistance of antennas at 13.56 MHz.

Antenna	Diameter (mm)	Height (mm)	Number of Turns	Pitch (mm)	Calculated Inductance (µH)	Calculated Resistance (Ω)	Q
Large emitter	26.5	10	6	1.38	1.29	0.77	143
Small emitter	15.5	10	9	0.84	1.13	0.61	157
Large receiver	22.5	5	4	0.86	0.59	0.52	97
Medium receiver	21.5	5	4	0.86	0.56	0.49	98
Small receiver	19.5	5	6	0.54	1.13	0.98	98

By implementing antenna dimensions in Equations (21) and (22) and using the inductances from Table 4 in Equation (27), we can calculate the coupling coefficient k of the several pairs. The condition is that the antenna must be superposed and concentric, giving Table 5:

Table 5. Coupling coefficient calculated of antennas at 13.56 MHz for concentric position.

Emitter	Receiver	Appellation	k
Small	Small	Small 1	0.57
Small	Medium	Small 2	0.49
Small	Large	Small 3	0.45
Large	Small	Large 1	0.47
Large	Medium	Large 2	0.56
Large	Large	Large 3	0.61

The modelled antennas are fabricated by winding copper wire with a diameter of 0.25 mm around 3D-printed supports and are presented in Section 3.1. The supports are printed using PETG and PLA materials.

We can then verify the models and extract S-parameters to perform simulations of power transfer. Those simulations use Keysight's Advanced Design System (ADS v2024 update 1.1) software. To measure power transfer, a oscilloscope LeCroy HDO6054B (Teledyne LeCroy, Chestnut Ridge, NY, USA) is used. For differential measurement, a 1P033 LeCroy differential probe (Chestnut Ridge, NY, USA) is used. For single-ended measurements, a PP023 LeCroy probe (Teledyne LeCroy, Chestnut Ridge, NY, USA) is used and connected to the board ground pins.

Impedance measurements are conducted using a Keysight E5061B (Keysight, Santa Rosa, CA, USA) Vector Network Analyzer (VNA), coupled with a directional coupler ZFBDC20-61HP+ (Mini-circuits, Brooklyn, NY, USA). To achieve high-power operations, a oscilloscope amplifier by Bowen (Keolabs, Grenoble, France) is employed.

The wireless power transfer system consists of the ST NFC chip transmitter and receiver.

Figure 1 shows the different steps of power transfer. The letters identify key steps of the transmission and are used as references in this article. Table 6 below shows the correspondence of the letters.

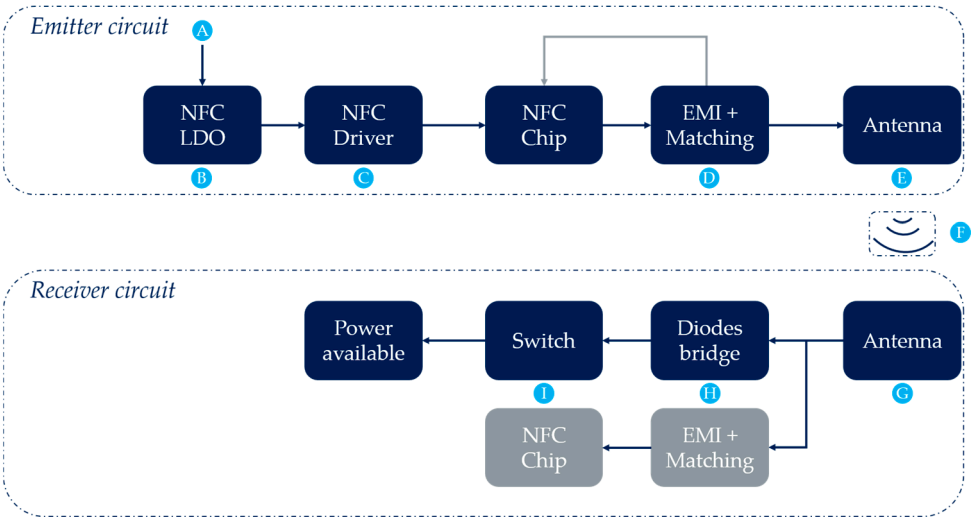


Figure 1. Power transfer circuit, from power supplied to transmission output.

The first steps A, B, and C of the emitter circuit are part of the chip used. This article does not provide detailed information regarding the values or technologies embedded.

Step "D" represents the circuit after the NFC chip. It is composed of a differential EMI filter circuit (inductance of 82 nH and a parallel capacitance of 680 pF on both side), and a differential matching circuit (two serial capacitances on each channel connected by a third parallel capacitance). The antennas represented in steps "E" and "G" can be simulated via

inductances. The parameters of these inductances represent the antenna characteristics calculated by using Equations (1)–(27) or measured using the VNA setup if the antennas are realized. In this configuration, R_s is the serial resistance of the inductance while L_s is the self-inductance value. Then, a mutual block is added to the simulation to incorporate the coupling coefficient linking both inductances. The coupling coefficient can be calculated or extracted from measurement.

Table 6. Association of steps in Figure 1.

Step	Part of the Power Transfer
A	Power source
B	Low drop out losses
C	Radio frequency output driver losses
D	Electromagnetic interference filter (EMI) and impedance matching losses
E	Emitter antenna losses
F	Coupling losses
G	Receiver antenna losses
H	Diode bridge losses
I	Switch on charging enabling losses

Another solution is to measure and implement the S2P parameter of the antenna pair. Step "H" is a bridge rectifier made of four diodes. Step "I" is a switch made of two NMOS and one PMOS, enabling the activation or deactivation of charging. The power available after the losses due to the switch (step "I") represents the power available at the end of the transfer. It is the power available to charge a battery or provide power to other components of the device.

Since the primary focus of this work is the electromagnetic design, coupling, and spatial integration of the 3D helicoidal antennas, the antenna parameters (presented in Table 3, Tables 11 and 12) and their coupling coefficients (Table 13) are fully reproducible. The active transmitter chip chain (Steps A to C) is treated as a proprietary driver delivering the operating power, and its specific microelectronic layout is outside the scope of this paper.

For simulation purposes, the physical setup is reproduced in the simulation environment. The antennas are characterized using a Vector Network Analyzer (VNA), and S-parameters are measured.

An alternative approach to simulate antenna behaviour involves measuring the antenna parameters at the target frequency, 13.56 MHz for NFC applications, followed by S_{21} parameter measurement at the same frequency. First, the Z-parameters are extracted from the S2P file. Subsequently, the resistive (R) and reactive (X) components of the impedance (Z) are obtained, as shown in Equation (28). Then, the antenna parameters can be extracted from S2P files using straightforward calculations (Equations (29)–(32)):

$$Z_{11} = R_{11} + jX_{11}. \tag{28}$$

From these parameters, the antenna characteristics can be extracted as a function of frequency f (Equations (29) and (30)):

$$L_{s_{11}} = \frac{X_{11}}{2\pi * f}, \tag{29}$$

$$R_{s_{11}} = R_{11}. \tag{30}$$

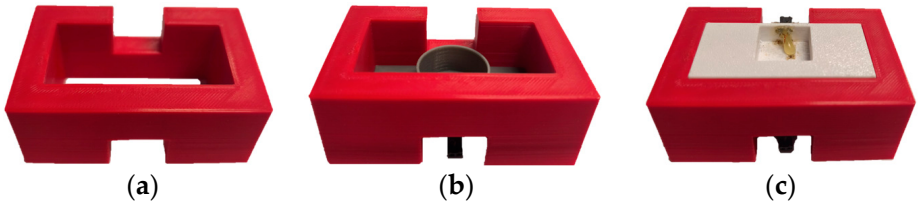
Equation (31) presents the formula provided by [25]:

$$k = \frac{M}{\sqrt{L_1 * L_2}}. \tag{31}$$

The application of Equations (29) and (31) results in Equation (32):

$$k = \frac{X_{21}}{\sqrt{X_{11} * X_{22}}}. \tag{32}$$

The shape of the antenna's 3D-printed support ensures a consistent antenna position during measurements, as shown in Figure 2.

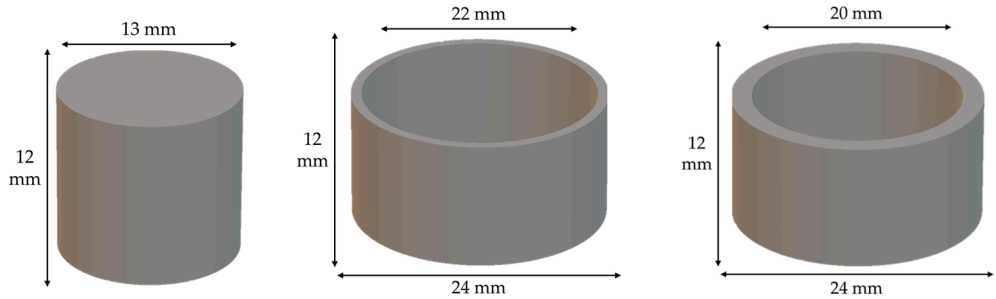


(**a**) (**b**) (**c**)

Figure 2. The 3D-printed alignment support (**a**) alone, (**b**) with only an emitter antenna (**c**) and with an antenna pair. Note: Minor variations in the 3D-printed support colour between white, or grey are due to different batches; all polymers (PETG/PLA) used during fabrication have negligible impacts on the electromagnetic behaviour of the antennas.

The antennas dimensioned at the beginning of Section 2 are fabricated. They represent two helical emitters (presented in Figure 4) and three helical receiver antennas (presented in Figure 5). The antennas differ in diameter, pitch, and number of turns. The largest receiver has fewer turns.

First, all antennas are individually characterized by extracting S_{11} parameters and the equivalent series circuit parameters (inductance L_S and resistance R_S). Subsequently, all emitter receiver pairs are measured with and without ferrite. Three ferrite shapes (Figure 3) corresponding to three different ferrite materials are evaluated. Their dimensions are indicated in Table 7.



(**a**) (**b**) (**c**)

Figure 3. Ferrite shapes. (**a**) Rod. (**b**) Thin tube. (**c**) Thick tube.

Table 7. Dimensions of different ferrite shapes.

Ferrite Shape	Outer Diameter (mm)	Inner Diameter (mm)	Height (mm)
Rod	13	0	12
Thin tube	24	22	12
Thick tube	24	20	12

The physical integration of ferrite materials, as described in Figure 3 or Table 7, within the operating volume of antennas significantly alters the electromagnetic behaviour of the inductive link between the emitter and receiver antennas [32]. The high magnetic permeability (μ_r) of the ferrites concentrates and channels the magnetic flux lines, shielding the system and mitigating magnetic leakage [33]. Consequently, both self-inductances (L) of the antennas and their mutual inductance (M_{12}) increase [34]. This phenomenon also improves the coupling coefficient of the antenna pairs if the ferrite surface is placed at the superposition of the fields of both antennas. However, adding ferrites at 13.56 MHz also induces effects in the ferromagnetic substrate such as eddy currents. It leads to an additional AC series resistance (R_{sAC}), impacting the antenna's resistance and quality factor. Balancing the enhancement in inductive parameters against quality factor deterioration, among other effects, such as increased Joule's effects, defines the boundaries required to optimize magnetic coupling without compromising the end-to-end efficiency.

The shapes of the printed antennas ensure that all receiver antennas have the same position in the operating volume of the emitter antenna.

At this point, the S2P file of the selected pairs is used to perform impedance matching at 2 W and 3 W and to simulate power transfer.

The input and output power of each step are extracted to estimate the losses of them. There are three exceptions:

The losses in the LDO are calculated by applying Equation (33) using the current and drop-out voltage of the chip component.

$$P_{LDO} = V_{LDO} * I_{LDO}. \tag{33}$$

Other exceptions are antennas; the losses are calculated by converting the peak voltage into RMS (root mean square) via Equation (34). Equation (35) extracts the parallel equivalent resistance of the antenna to consider the whole antenna as a resistor. It enables the calculation of the Joule's effect losses with Equation (36).

$$V_{RMS} = \sqrt{\frac{1}{T}\int_0^T v(t)^2 t}, \tag{34}$$

$$R_p = \frac{(\omega L_s)^2}{R_s}, \tag{35}$$

$$P_{joule} = \frac{{V_{RMS}}^2}{R_p}. \tag{36}$$

The last exception is the coupling losses. They are recalculated in Equation (37) using the power available at each antenna, the losses in each antenna and the power available.

$$P_{Coupling} = P_{EmitterAvailable} - P_{EmitterAnt} - P_{Receiver} - P_{ReceiverAnt} - P_{OutAvailable}. \tag{37}$$

Then, the antennas pairs are matched, and the power transfer is measured to confirm the simulations. The measured losses are extracted from the measurements made on the board. All measurements are performed in differential between the two lines of the system using a differential probe. After the diode bridge, the measurement is performed using a regular single probe. All voltages are measured in rms values. Currents are measured with portable multimetres to perform non-intrusive measurements (without ground noise from the bench power supply). The batteries are connected to avoid the usage of direct current (DC) power supply and ground noise. The usage of the differential probe makes it possible to bypass ground noise during differential measurement. It might have a light impact for DC voltage measurement after the diode bridge. Below are the calculations for each step of the power transfer:

Estimation of the source power is performed with Equation (38). It uses the internal driver resistance, the output driver impedance, and the driver's source voltage.

$$P_{ScMeas} = \left(\frac{\sin\left(\pi * \frac{Step}{2*Step_{Max}}\right)}{R_{Load} + 2 * R_{OutDriver}} * V_{ScDriver} * \frac{2 * \sqrt{2}}{\pi} \right)^2 * (R_{Load} + 2 * R_{OutDriver}). \quad (38)$$

The losses due to the low drop-out are extracted from the chip driver's current and the theoretical drop-out voltage, as shown in Equation (39).

$$P_{LDOLosses} = \left(\frac{\sin\left(\pi * \frac{Step}{2*Step_{Max}}\right)}{R_{Load} + 2 * R_{OutDriver}} * V_{ScDriver} * \frac{2 * \sqrt{2}}{\pi} \right) * V_{LDOth}. \quad (39)$$

The losses due to the driver's resistance are extracted from the chip driver's current and internal resistance, as shown in Equation (40).

$$P_{RFOLosses} = \left(\frac{\sin\left(\pi * \frac{Step}{2*Step_{Max}}\right)}{R_{Load} + 2 * R_{OutDriver}} * V_{ScDriver} * \frac{2 * \sqrt{2}}{\pi} \right)^2 * (2 * R_{OutDriver}). \quad (40)$$

The losses due to the chip's input driver are not considered in this article (in grey in Figure 1). This article is focused exclusively on wireless power transfer applications without communication. However, it could be calculated from the driver's internal and external resistances and the voltage at the antenna connected to those resistances. Equation (41) below shows the losses.

$$P_{Input_{driverLosses}} = \frac{\frac{V_{RMSAnt}}{(2*R_{InDriverext}+R_{InDriverint})}}{2}. \quad (41)$$

The losses due to the EMI filter are extracted using the driver's output current and the filter inductance's parasitic serial resistance, as shown in Equation (42) below.

$$P_{EMILosses} = \left(\frac{\sin\left(\pi * \frac{Step}{2*Step_{Max}}\right)}{R_{Load} + 2 * R_{OutDriver}} * V_{ScDriver} * \frac{2 * \sqrt{2}}{\pi} \right)^2 * (2 * R_{EMI}). \quad (42)$$

Equation (43) shows the antenna losses. The antenna voltage and the equivalent parallel resistance, which is estimated with Equation (35), are used to calculate these losses.

$$P_{AntLosses} = \frac{{V_{AntRMS}}^2}{R_{pAntEq}} \quad (43)$$

Equation (44) extracts the losses due to the diode bridge, using the output current of the diode bridge and the forward voltage threshold of the diodes.

$$P_{Bridge} = 2 * V_{Fdiode} * I_{Bridgeout} \quad (44)$$

The switch's losses are extracted from Equation (45) below, using the current at the output of the bridge and the resistance drain source of the PMOS used.

$$P_{Switch} = R_{DSon} * {I_{Bridgeout}}^2 \quad (45)$$

The coupling losses are estimated from the total emitter and receiver losses, the source power, and the available power, as shown in Equation (46) below.

$$P_{CouplingLosses} = P_{ScMeas} - P_{EmitLosses} - P_{ReceivLosses} - P_{Available_Out} \quad (46)$$

Available power is calculated from the output current and voltage of the transmission, as shown in Equation (47) below.

$$P_{Available_Out} = I_{Out} * V_{RMSOut} \quad (47)$$

Table 8 is a summary of all parameters used in Equations (38)–(47) above.

Table 8. Parameters of wireless power transfer at 2 W and 3 W.

Parameter	Value for 2 W Transmission	Value for 3 W Transmission	Units
Source voltage	6.25	7.60	V
Driver resistance	0.40	0.40	Ω
LDO voltage drops	0.20	0.20	V
EMI inductance	82.00	82.00	nH
EMI capacitance	680.00	680.00	pF
Matching serial capacitance	Depends on antenna	Depends on antenna	pF
Matching parallel capacitance	Depends on antenna	Depends on antenna	pF
Forward voltage of diode	0.36	0.36	V
Switch resistance RDSON	0.33	0.33	Ω
Aimed load of NFC chip	13 − 1j	13 − 1j	Ω
Output load	Depends on charging current	Depends on charging current	Ω

Table 9 indicates the simulated values of the matching network for each antenna pair. The charging current defined is 50 mA.

Table 9. Values of matching capacitances and output load for wireless power transfer at 2 W and 3 W.

Pair	Power	C_s (pF)	C_p (pF)	Load (Ω)
Small 1	2 W	213	90	110
Small 2	2 W	232	33	110
Small 3	2 W	196	69	110
Large 1	2 W	145	60	110
Large 2	2 W	179	73	110
Large 3	2 W	212	33	110
Small 1	3 W	186	111	110
Small 2	3 W	165	83	110
Small 3	3 W	180	81	110
Large 1	3 W	136	65	110
Large 2	3 W	213	49	110
Large 3	3 W	193	48	110

Table 10 indicates the values of the matching network for “Small 1”, “Small 2”, and “Large 1” pairs used for the simulation and measurement with alternative configurations. The charging current used remains at 50 mA.

The values used in Tables 9 and 10 correspond to the components used to match the NFC chip output load as closely as possible to the target specifications defined in Table 8. The discrepancies between the simulated and practically implemented values are due to the available capacitances’ values.

Table 10. Values of matching capacitances for wireless power transfer simulation and measurement at 3 W.

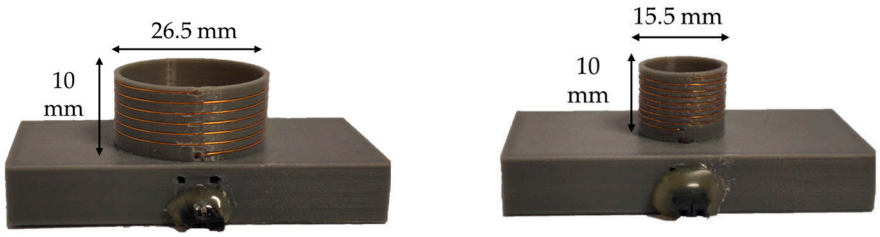
Pair	Method	C_s (pF)	C_p (pF)
Small 1	Simulated	191	91.0
Small 2	Simulated	176	79.0
Large 1	Simulated	137	64.0
Small 1	Measured	280	79.0
Small 2	Measured	192	52.6
Large 1	Measured	146	64.0

The matching methodology consists of first simulating the power transfer using measured S2P antenna files. Then, the matching network is set to match the target specification impedance at the output of the chip. The prototype board is then assembled with the closest component values possible. The matching is modified to reach the closest impedance to the target value. Finally, simulation matching is adjusted to provide an NFC chip output load impedance similar to the measured value.

3. Results

3.1. Antennas

This paper provides a summary of the different emitter antennas' dimensions and characteristics. For the sake of simplicity, the antennas are named "Large emitter" (Figure 4a) and "Small emitter" (Figure 4b).



(**a**) (**b**)

Figure 4. Prototype emitter antennas. (**a**) Large emitter antenna; (**b**) small emitter antenna. Note: Minor variations in the 3D-printed support colour grey is due to different batch; all polymers (PETG/PLA) used during fabrication have negligible impacts on the electromagnetic behaviour of the antennas.

3.1.1. Emitter Antennas

Table 11 shows the different antennas' dimensions and their characteristics.

Table 11. Dimensions and characteristics at 13.56 MHz of emitter antennas.

Antenna	Diameter (mm)	Height (mm)	Number of Turns	Pitch (mm)	Support Material	Inductance (µH)	Resistance (Ω)	Q
Large emitter	26.5	10	6	1.38	PETG	1.27	0.85	127
Small emitter	15.5	10	9	0.84	PETG	1.00	0.78	109

Both emitter antennas are represented in Figure 4 below. The large emitter antenna is the one used in Figure 2b.

The measurements performed on the emitter prototypes reveal values close to those calculated in Section 2.2, thereby validating the models used for these applications.

3.1.2. Receiver Antennas

The following is a summary of the different receiver antennas' dimensions and characteristics. The measurements performed on the receiver prototypes reveal values close to those calculated in Section 2.2., thereby validating the models used for these applications.

There are three different receivers. One is small, similar to the small emitter; the two others are closer to the large emitter. For the sake of simplicity, these antennas are named "Large receiver" (Figure 5a), "Medium receiver", and "Small receiver" (Figure 5b) in this paper.

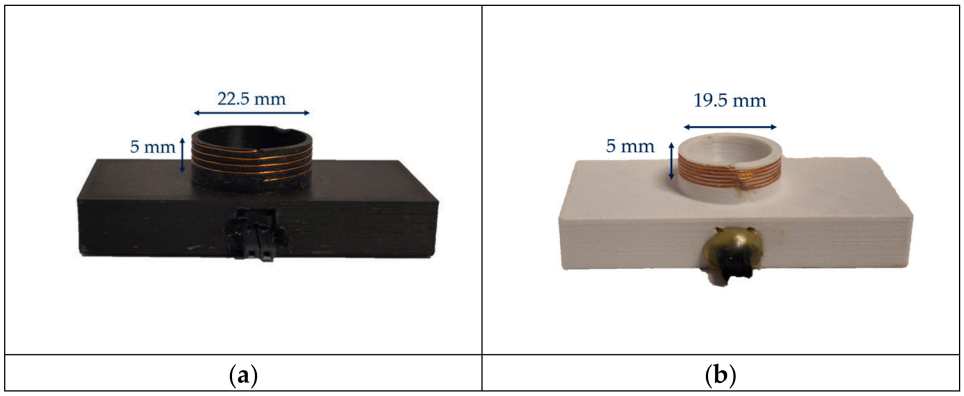


Figure 5. Prototype receiver antennas. (**a**) Large receiver antenna; (**b**) small receiver antenna. Note: Minor variations in the 3D-printed support colour between white or black are due to different batches; all substrate polymers (PETG/PLA) used during fabrication have negligible impacts on the electromagnetic behaviour of the antennas.

Table 12 shows the different antennas' dimensions and their characteristics.

Table 12. Dimensions and characteristics at 13.56 MHz of receiver antennas.

Antenna	Diameter (mm)	Height (mm)	Number of Turns	Pitch (mm)	Support Material	Inductance (µH)	Resistance (Ω)	Q
Large receiver	22.5	5	4	0.86	PLA	0.59	0.51	99
Medium receiver	21.5	5	4	0.86	PETG	0.56	0.49	97
Small receiver	19.5	5	6	0.54	PETG	1.10	0.90	104

Two of the receiver antennas are represented below. The small receiver antenna is also the one used in Figure 2c. The antennas are 3D-printed, with different batches, so the colour may change but the materials are similar in terms of electromagnetic behaviour.

3.1.3. Antenna Pair Measurements

The different emitters are measured with all receiver antennas. All measurements are performed with the VNA and the same parameters. Table 13 presents the emitter and receiver antennas, the S12 parameter at 13.56 MHz and the calculated coupling coefficient "k" that is represented in Figure 6. The materials used for 3D printing have almost no impact on the antenna characteristics, as indicated by [35,36]. This is confirmed by the negligible difference between the values in Tables 4 and 11–13.

The coupling coefficient displays a difference of 5% with the estimated coupling coefficient in Section 2.2. All of the modelled parameters are validated by measurements. Some differences are still present due to the accuracy of the measurements and the 3D printing process. The model and realization are precise enough for the applications in this article. These applications focus on power transfer and end-to-end efficiency with the NFC 3D-shaped antenna design.

Table 13. Coupling coefficient of antennas at 13.56 MHz.

Emitter	Receiver	Appellation	k	Distance (mm)
Small	Small	Small 1	0.58	2.00
Small	Medium	Small 2	0.48	3.10
Small	Large	Small 3	0.45	3.50
Large	Small	Large 1	0.47	3.50
Large	Medium	Large 2	0.56	2.40
Large	Large	Large 3	0.60	2.00

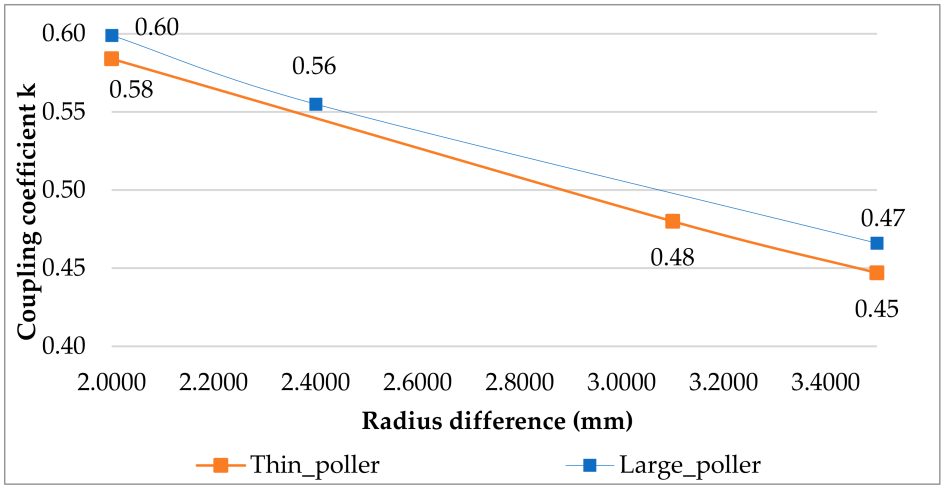


Figure 6. Coupling coefficient depending on radius difference for thin and large emitters.

The radius difference represents the distance between the antennas for concentric solenoids. The analysis of the distance impact on the coefficient coupling is represented in Figure 6.

The application of ferrite rods as shown in Figure 3a at the centre of the coils has an impact on the coupling coefficient, as shown in Table 14.

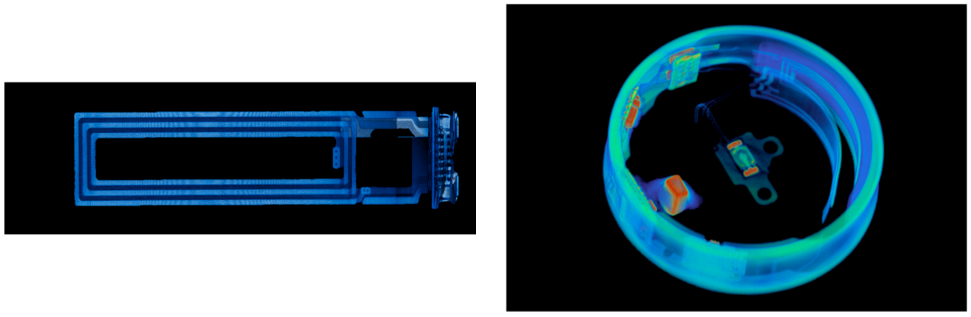
Table 14. Coupling coefficient of antennas at 13.56 MHz with E11 ferrite rods.

Pair	k	Distance (mm)	Ferrite Surface (mm^2)	Emitter Surface (mm^2)
Small 1	0.79	2.00	132.73	188.69
Small 2	0.70	3.10	132.73	188.69
Small 3	0.67	3.50	132.73	188.69
Large 1	0.62	3.50	132.73	551.55
Large 2	0.70	2.40	132.73	551.55
Large 3	0.67	2.00	132.73	551.55

3.1.4. Representative Planar Reference Antennas

As mentioned in the introduction, a typical use case for NFC charging is the ring. In [9], a scan of a well-known product is provided, as shown in Figure 7a,b. This is the type of antenna referred to as the reference antenna in this article.

From the images available in [9], the dimensions of the antennas can be estimated at 20.5 mm × 4 mm for the ring antenna and 20 mm × 4.5 mm for the case antenna. Those values represent a similar surface area compared to the reference antenna pair present in the standards. Therefore, the antennas presented in Table 15 can be used as representative planar reference antennas. These planar antennas are conformal to the shape of the packaging. In this manuscript, the pair used for this configuration will be called "planar reference". Table 15 below indicates the measured parameters of these antennas:



(**a**) (**b**)

Figure 7. Well-known market product antennas obtained with computed tomography scans. (**a**) Ring antenna. (**b**) Case antenna and ring. Obtained from [9].

Table 15. Dimensions and characteristics of representative planar reference antennas at 13.56 MHz.

Antenna	Length (mm)	Width (mm)	Number of Turns	Pitch (mm)	Material	Track Width (mm)	Track Thickness (mm)	Inductance (µH)	Resistance (Ω)	Q
Emitter	23.0	4.85	2	0.15	Copper	0.5	0.07	0.11	0.34	27
Receiver	20.3	5.30	3	0.15	Copper	0.3	0.07	0.22	0.52	36
Emitter + Ferrite MQ15	23.0	4.85	2	0.15	Copper	0.5	0.07	0.15	0.39	32
Receiver + Ferrite MQ15	20.3	5.30	3	0.15	Copper	0.3	0.07	0.33	0.68	41

These antennas are used for the following simulations. They are evaluated under a similar operating setup as that of the prototype antennas; the matching values are modified to obtain similar impedance at the output of the NFC chip. The planar reference antennas are made on PCB with rectangular tracks. The substrate is a 0.8 mm thick FR4 substrate. These antennas represent a pre-existing reference of normative antennas for small wearable NFC wireless charging applications. As such, they existed prior to this study and were not specifically developed for this work, allowing them to serve as an independent baseline. The parameters indicated in Table 15 have been measured with the same VNA configurations as the measured parameters of the prototype antennas in Tables 11 and 12. The dimensions in Table 15 have been extracted from the antennas of Gerber's files.

The coupling coefficient of these antennas decreases as the gap between the antennas increases. Table 16 below shows this variation.

Table 16. Coupling coefficient of reference antennas at 13.56 MHz depending on distance.

Emitter (mm)	Receiver (mm)	k	Distance (mm)
23 × 4.85, 2 turns	20.3 × 5.3, 3 turns	0.31	0.75
		0.19	1.50
		0.12	2.25
		0.08	3.00
		0.06	3.75
		0.05	5.00

Measurements were also performed for the reference antennas with a ferrite sheet. Their coupling coefficient fluctuates, as shown in Table 17.

Table 18 below represents all antenna values, both simulated and measured.

Table 17. Coupling coefficient of reference antennas at 13.56 MHz depending on distance with MQ15 ferrite sheet.

Emitter (mm)	Receiver (mm)	k	Distance (mm)
23 × 4.85, 2 turns	20.3 × 5.3, 3 turns	0.39	0.75
		0.24	1.50
		0.15	2.25
		0.11	3.00
		0.08	3.75
		0.06	5.00

Table 18. Simulated and measured antenna characteristics.

Antenna	Simulated Inductance (µH)	Simulated Resistance (Ω)	Simulated Q	Measured Inductance (µH)	Measured Resistance (Ω)	Measured Q
Large emitter	1.29	0.77	143	1.27	0.85	127
Small emitter	1.13	0.61	157	1.00	0.78	109
Large receiver	0.59	0.52	97	0.59	0.51	99
Medium receiver	0.56	0.49	98	0.56	0.49	97
Small receiver	1.13	0.98	98	1.10	0.90	104
Planar emitter	X	X	X	0.11	0.34	27
Planar receiver	X	X	X	0.22	0.52	36

3.2. First Power Transfer Simulations

The objective of these simulations is to predict the physical power variation and end-to-end efficiency of the power transfer, as well as to localize the steps presenting the primary losses. For this study, a target validation threshold of 5 percentage points is defined for the absolute agreement between the simulated and measured overall end-to-end efficiency. This target is mathematically and physically justified by the tolerance of the passive components in the matching network and EMI filter (Step "D"). These are made of two successive components each. Since each individual SMD component has a manufacturer tolerance of ±2%, the worst-case cumulative tolerance of these blocks alone can reach up to 4% relative error. We round this value to a 5 percentage point difference. This represents an ideal threshold that does not account for additional experimental sources of error, such as VNA measurement tolerances, differential probe calibration uncertainties, or manual positioning of the prototype coils. Nevertheless, the custom alignment support shown in Figure 2 is designed to ensure a highly reproducible concentric alignment between the transmitter and receiver antennas.

It is important to emphasize that this 5% criterion is applied strictly to the overall end-to-end power transfer efficiency, which represents the primary focus of this study. The individual step-level losses are not bound by this strict criterion, as cumulative modelling and measurement uncertainties tend to concentrate within intermediate steps, particularly from Step "E" onward. These deviations may result from variations in the antenna electrical characteristics, coupling efficiency, dynamic power circulation, and Joule's effects.

To simulate the antenna pairs, S-parameters files are used. To obtain the most valuable comparison, the distance between the reference antennas is 0.75 mm. It is the distance showing the highest coupling coefficient, as shown in Tables 16 and 17.

The first pair realized is the "Small 1" pair. It is used for an end-to-end power transfer comparison with the reference antenna pair. First, the comparison is made at 2 W and then a second comparison is performed at 3 W. In both cases, the power source is fixed, and the impedance matching indicates similar impedances. The power emitted is indicated at the output of the NFC chip. The coupling coefficient of the antennas is extracted from the S2P measurements. These simulations are made for wireless charging exclusively. This choice enables reaching the maximum power available at the output of the circuit.

3.2.1. Simulation of the End-to-End Power Transfer at 2 W

Figure 8 represents the power budget using the prototype pair "Small 1" and the planar reference pair for a power transfer at 2 W. In the present work, "power budget" defines the evolution of the power available at each step of the power transfer from the power supply to the output power available.

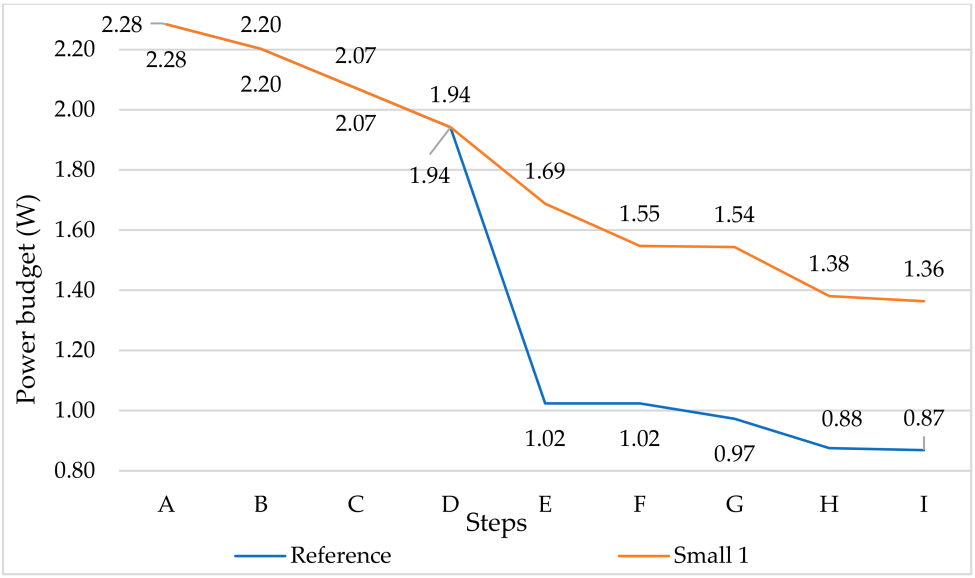
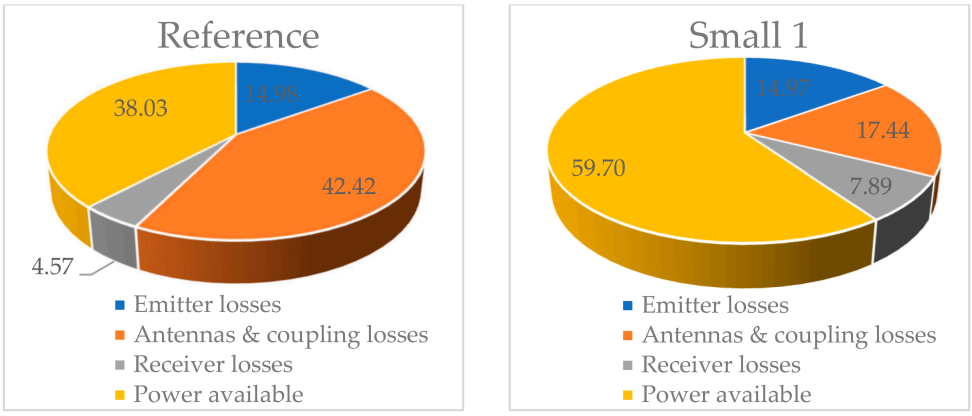


Figure 8. Power transfer at 2 W for representative planar reference pair and prototype antenna pair "Small 1".

It shows that the power at the source (Step "A") is equivalent at 2.28 W, reaching 2.0 W at the NFC chip output. The losses due to the chip, the EMI filter, and impedance matching are also similar, as they depend on the supplied power rather than antenna selection. Between Step "E" and Step "I", a 56.3% relative increase in the power received is reached by using the "Small 1" pair antenna. The power increases from 0.87 W with the planar reference antennas to 1.36 W with the prototype antennas.

The pie charts in Figure 9a,b show the source power lost in different areas. They include losses in the emitter, antennas, and coupling in the receiver. The charts also display the power that is available at the end of the transmission. For the 2 W simulations, the end-to-end efficiency achieves a total 22 percentage point improvement (from 38% to 60% end-to-end efficiency) with "Small 1" instead of the reference pair.



(**a**) (**b**)

Figure 9. Power repartition at 2 W for system. (**a**) Using planar reference pair. (**b**) Using prototype antenna pair.

In Figure 9, the improvement in the available power for the circuit or to charge a battery is higher (21.67% difference). The power lost in the antennas and coupling is lower (24.98% difference). This improvement shows that the objective of the 3D antenna design is achieved.

3.2.2. Simulation of the End-to-End Power Transfer at 3 W

The simulation at 3 W shown in Figure 10 indicates the same power transfer behaviour as the test at 2 W.

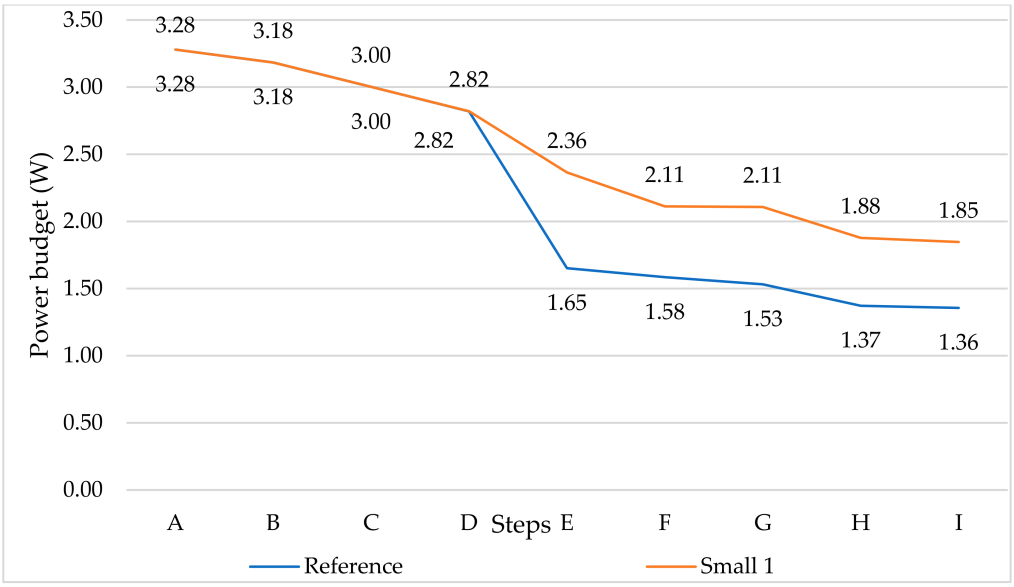
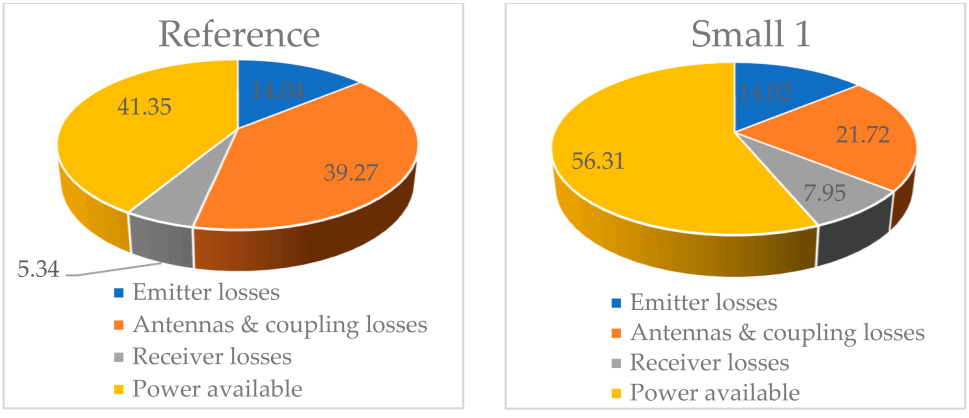


Figure 10. Power transfer at 3 W for planar reference and prototype antenna pair "Small 1".

An increase in the losses in the first steps of each configuration is present. This is due to the amount of power being higher. This causes an increase in the amount of power dissipated by Joule's effect. Despite this increase, the losses from Steps "A" to "D" are still similar for both pairs. The amount of power dissipated at each step increases. The power available at Step "I" is still better with the prototype, reaching 1.85 W instead of 1.36 W for the planar reference pair. This represents a relative increase of 36% in the final available power with the "Small 1" pair compared to the representative planar reference pair.

The pie charts presented in Figure 11a,b are made of the same groups as in Figure 9a,b. They show the global improvement due to the solution.



(**a**) (**b**)

Figure 11. Power repartition at 3 W for system. (**a**) Using planar reference antennas. (**b**) Using prototype antenna pair "Small 1".

At 3 W, the power available at the end of the transmission is improved for the reference compared to the 2 W transmission. For the prototype "Small 1", the available power is less, with 56% of the source power transmitted against 60% at 2 W. But the end-to-end transmission at 3 W is still more efficient with the prototype (56%) than the reference (41%). It represents a 15 percentage point gain in end-to-end power transfer efficiency.

3.3. Power Transfer Measure

To check the simulation, the "Small 1" pair is connected to boards used for NFC charging. The setup used in the simulation is reproduced to compare the losses measured to the losses simulated. Figure 12 shows the power budget of the pair "Small 1" in simulation and in measurement. The gap between the measured and simulated end-to-end efficiency must comply with the 5 percentage point maximum difference criterion defined at the beginning of this section.

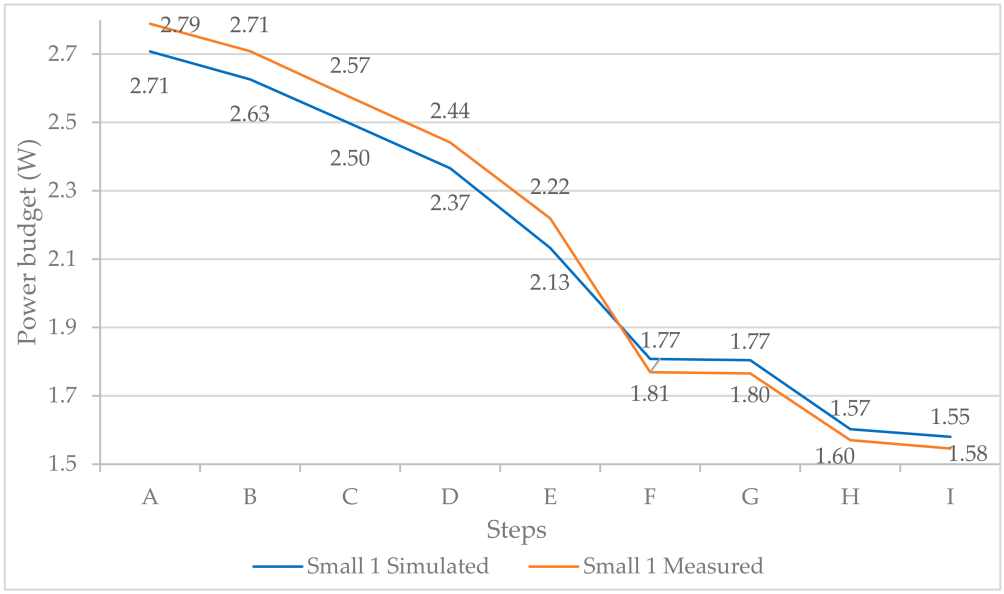


Figure 12. Comparison of simulated and measured power budget for "Small 1" pair.

Both curves remain parallel. This indicates equivalent losses at each step in simulation and in measurement. The steps showing a difference between measurement and simulation are Steps "E" to "G", involving the emitter antenna, the coupling losses, and the receiver antenna. The difference can be explained by the way the S2P file is measured. The antennas are nested in a concentric way without any other components connected. The measurement is performed at 0 dBm. During the measurement, the diode bridge is connected, introducing non-linear behaviour, and the power going through the antennas is different from 0 dBm. The loss difference of these three points is displayed in Table 19 below.

From these values, we can calculate both end-to-end efficiencies. The simulation efficiency is 55.56%. The measured efficiency is 58.30%. The difference between those two efficiencies is 2.74 percentage points or a 4.94% relative error. The criterion chosen due to the power transfer architecture is 5 percentage points. The simulation is still in line with this criterion. Furthermore, the coupling losses are dependent on the antennas' losses and the power available. There is still an important difference in the coupling losses (Step "F"). This is due to the calculation of these losses, presented in Equation (37). This calculation inherits the uncertainties stemming from the measurement and modelling of the whole power transfer. The calculation of the coupling losses is also affected by the receiver antenna not being tuned. It generates losses that are included in the coupling due to receiver antennas. Therefore, it does not invalidate the accuracy of the simulation.

Table 19. "Small 1" pair analysis of simulation and measurement differences.

Step	Losses in Simulation (W)	Losses in Measurements (W)	Flat Difference (mW)	Absolute Difference (%)	Step Yield Simulated (%)	Step Yield Measured (%)	Percentage Points Difference	Relative Yield Difference (%)
A	2.79	2.71	80	2.87	X	X	X	X
B	2.71	2.63	80	2.95	97.13	97.05	0.08	0.09
C	2.57	2.50	70	2.72	94.83	95.06	0.22	0.24
D	2.44	2.37	70	2.87	94.94	94.80	0.14	0.15
E	2.22	2.13	90	4.05	90.98	89.87	1.11	1.22
F	1.77	1.81	40	2.26	79.73	84.98	5.25	6.58
G	1.77	1.80	30	1.69	100.00	99.45	0.55	0.55
H	1.57	1.60	30	1.91	88.70	88.89	0.19	0.21
I	1.55	1.58	30	1.94	98.73	98.75	0.02	0.02
End-to-end efficiency (%)	55.56%	58.30%	X	4.94%	55.56%	58.30%	X	X

Consequently, the simulation is validated as a reliable tool for end-to-end power transfer estimations and comparison because of the simulation being highly representative of the physical measurements.

3.4. Power Transfer Simulation

3.4.1. Power Transfer Simulation at 2 W

Figure 13 compares the simulation at 2 W of all the prototype pairs presented in Table 5.

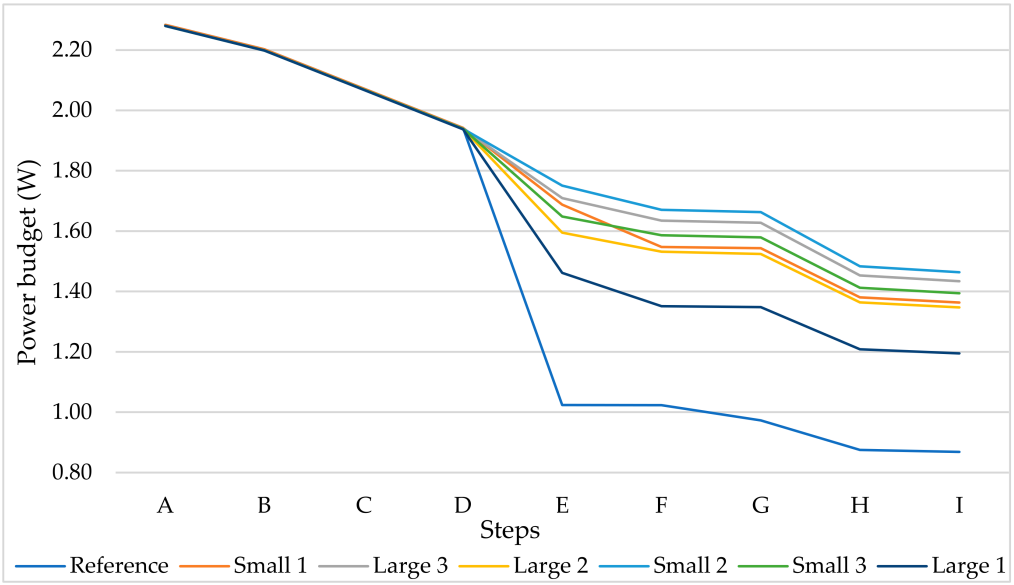


Figure 13. Power transfer at 2 W for all antenna pairs.

All the simulations have the same source power applied and the same losses from Steps "A" to "D". The impedance matching of each simulation allows us to obtain the same power source at Step "A", namely 2.28 W. This power source with a drop-out voltage of 0.2 V at Step "B" provides 2.0 W at Step "C", designating the NFC chip output. The losses due to the EMI filter and impedance matching at Step "D" are the same for every pair if the chip configuration is the same. The antenna pair are not the same, so their characteristics indicated in Tables 11 and 12 vary, causing voltage fluctuations and equivalent resistance R_p shifting. This generates different losses for every antenna at Steps "E" and "G". The coupling coefficient of each pair is different, as indicated in Table 13, explaining the loss difference at Step "F". From this point, all the voltages are different. This is due to the

power source being transmitted by the emitter antenna to the "receiver" part via non-perfect coupling.

Table 20 shows the average losses of all prototype pairs, their standard deviation, and the reference values.

Table 20. Statistics of the losses of the 2 W power transmission compared to the reference values.

Step	Average (mW)	Standard Deviation (mW)	Reference Flat Value (mW)
A	0.00	0.00	0.00
B	81.68	0.07	81.60
C	129.87	0.29	130.20
D	130.02	0.27	130.30
E	296.95	93.49	918.00
F	88.43	28.40	0.10
G	6.18	2.02	50.70
H	163.87	12.60	97.70
I	17.25	2.02	6.60

Table 20 confirms the similarity of Steps "A" to "D" for all pairs. The proposed prototypes exhibit low standard deviations. This indicates great performance for various 3D geometries. The losses represented in Step "E" are due to the Joule's effect at the emitter antenna. The proposed antenna design achieves an average emitter loss reduction of 67.6% (reducing Step "E" losses from 918 mW with the planar reference to an average of 296.95 mW for the prototypes). However, the losses of the receiver are higher with the prototype than the planar reference. This phenomenon is due to the increase in the power successfully coupled and transferred to the receiver side.

The average end-to-end total losses of the prototypes are 0.91 W or 60% end-to-end efficiency, compared to 1.42 W or 38% end-to-end efficiency for the planar reference. The average absolute gain of end-to-end efficiency achieved with the 3D prototypes is 22 percentage points at 2 W.

It is also important to note the increase in Step "F" average loss (representing coupling losses) with the prototypes compared to the planar reference. This increase is due to the method used in Equation (37). The planar reference antenna is subject to important Joule's effect losses at the emitter antenna. This implies a reduction in the absolute power entering Step "F". Consequently, even with a lower coupling coefficient k, the absolute amount of power dissipated is lower than the amount of power dissipated with the prototype antennas. This phenomenon demonstrates the importance of comparing antenna pairs in terms of the coupling coefficient k or the absolute power dissipated during power transmission.

3.4.2. Power Transfer Simulation at 3 W

All of the prototype pairs presented in Table 5 have been simulated. All of the power transfers represented at 3 W are presented in Figure 14 below.

All the simulations have the same power supplied from Steps "A" to "D". The impedance matching of each simulation allows us to obtain the same power source at "A", namely 3.28 W. This power source with a drop-out voltage of 0.2 V at "B" allows the chip to obtain 3.0 W at Step "C". The losses due to the EMI filter and matching at Step "D" are the same for every pair. The antenna pair are not the same, so their characteristics indicated in Tables 11 and 12 vary, causing voltage variations and equivalent resistance R_p variations. This generates different losses for every antenna at Steps "E" and "G". The coupling coefficient of each pair is different as indicated in Table 13, explaining the loss difference at Step "F". From this point, all the voltages are different. This is due to the power source being transmitted by the emitter antenna to the "receiver" part via non-perfect coupling.

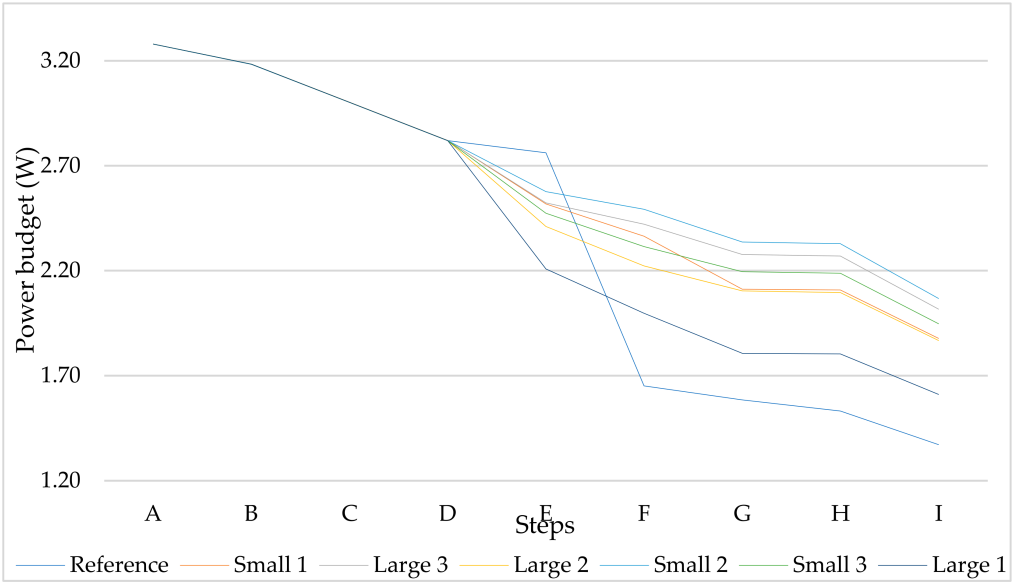


Figure 14. Power transfer at 3 W for all antennas pairs.

Table 21 below shows the average losses of all prototype pairs, their standard deviation, and the reference values.

Table 21. Statistics of the losses of the 3 W power transmission compared to the reference values.

Step	Average (mW)	Standard Deviation (mW)	Reference (mW)
A	0.00	0.00	0.00
B	96.63	0.05	96.50
C	181.70	0.14	181.80
D	182.02	0.11	182.10
E	517.62	160.20	1168.20
F	163.60	46.63	66.90
G	6.38	2.09	52.90
H	233.95	21.82	159.80
I	31.32	4.45	15.50

Table 21 confirms the similarity of Steps "A" to "D" for all pairs. The different prototypes exhibit low standard deviations, indicating that the 3D prototypes display similar behaviour no matter the antennas' dimensions. The losses at Step "E", caused by the emitter antenna's Joule's effect, are significantly lower with the proposed prototypes than with the planar reference antennas, resulting in an average reduction of 55.7% in emitter dissipation compared to the representative planar reference (reducing the loss from 1168.20 mW to an average of 517.62 mW). However, the losses due to the receiver side are higher with the prototype antennas than with the planar references. This is due to the amount of power transferred to the receiver side being higher.

The prototypes' average total loss is 1.41 W or 57% end-to-end efficiency, compared to 1.92 W or 41% end-to-end efficiency for the planar reference. The average absolute gain in end-to-end efficiency achieved by the proposed 3D antenna shapes is 16 percentage points at 3 W.

3.5. Behaviour Validation at 3 W

In the simulation of Section 3.4, we have observed that the "Small 2" pair performs best, while the "Large 1" pair is the worst case, and the "Small 1" pair corresponds to standard performance for the prototype pair. This is why a comparison with the measurement at 3 W

of the "Small 2" and "Large 1" pairs was performed to validate the simulation behaviour compared with the real measurement using different antenna sizes and pairs. The "Small 2" pair comparison is represented in Figure 15 below.

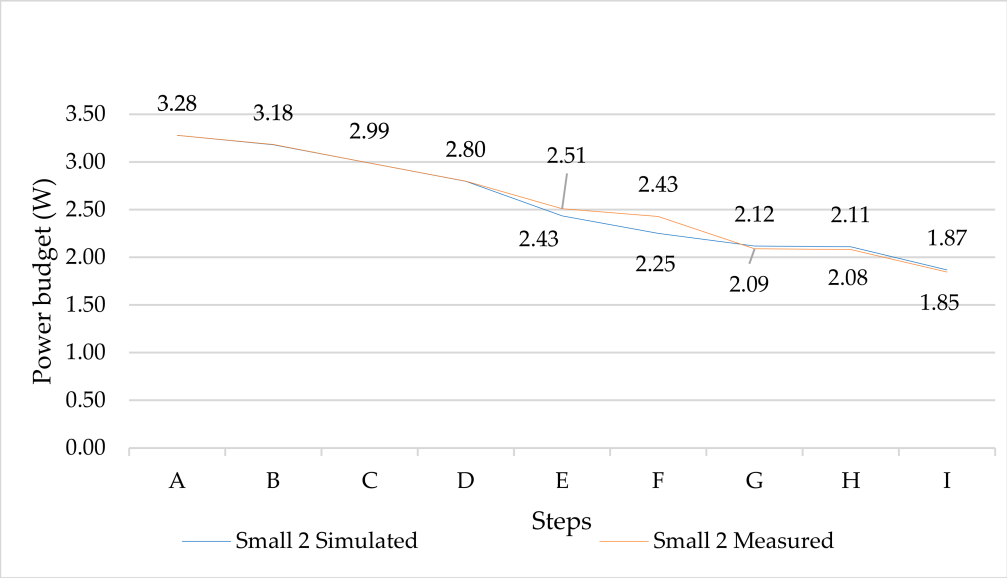


Figure 15. Comparison of simulated and measured power budget for "Small 2" pair.

The configuration is not the same as the measurement shown in Figure 12, as the power supply losses have been reduced. This enables us to reach 3.28 W at source in measurement and in simulation. But the losses are similar at each step, proving that the simulation matches the measurements if the input parameters are similar (source power, impedance fixed with matching circuit, antennas parameters). Table 22 presents the differences between the simulation and measurement.

Table 22. "Small 2" pair analysis of simulation and measurement differences at 3 W.

Step	Losses in Simulation (W)	Losses in Measurements (W)	Flat Difference (mW)	Absolute Difference (%)	Step Yield Simulated (%)	Step Yield Measured (%)	Percentage Points Difference	Relative Yield Difference (%)
A	3.28	3.28	0	0.00	X	X	X	X
B	3.18	3.18	0	0.00	96.95	96.95	0.00	0.00
C	2.99	2.99	0	0.00	94.03	94.03	0.00	0.00
D	2.80	2.80	0	0.00	93.65	93.65	0.00	0.00
E	2.43	2.51	80	3.29	86.79	89.64	2.86	3.29
F	2.25	2.43	180	8.00	92.59	96.81	4.22	4.56
G	2.12	2.12	0	0.00	94.22	87.24	6.98	7.41
H	2.08	2.11	30	1.44	98.11	99.53	1.42	1.44
I	1.85	1.87	20	1.08	88.94	88.63	0.32	0.36
End-to-end efficiency (%)	56.40%	57.01%	X	1.08%	56.40%	57.01%	X	X

Table 22 proves that the simulation and measurement are almost the same. Furthermore, solving the supply power reduces the difference between the simulation and measurements. The coupling Step "F" still has a high difference; adding a tuning capacitance to the receiver antenna would reduce these inconsistencies. The simulation is again in tune with the criterion of 5% difference regarding the end-to-end efficiencies.

Figure 16 validates the same analysis for the "Large 1" pair.

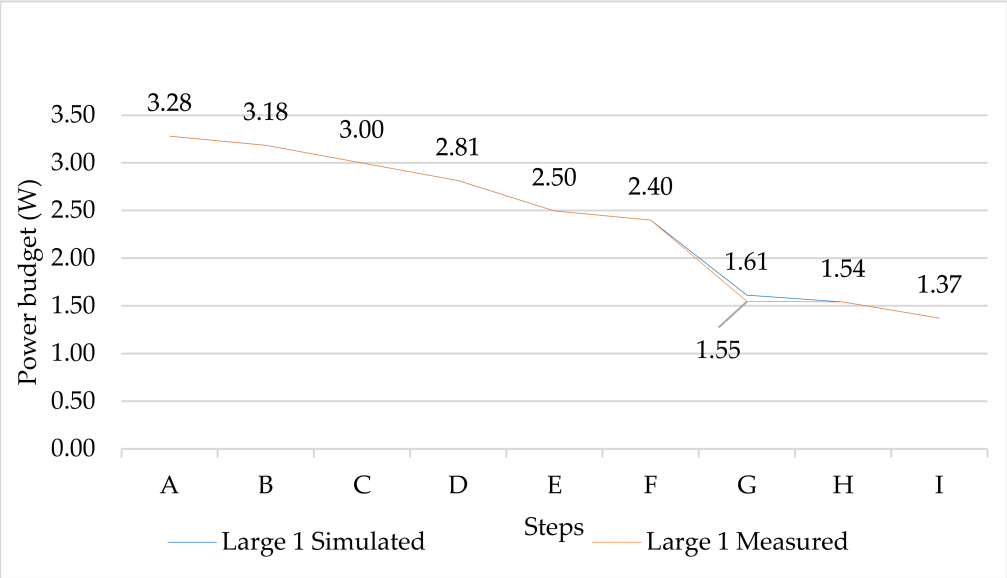


Figure 16. Comparison of simulated and measured power budget for "Large 1" pair.

In this comparison, both power transfers display the same losses. Once again, the simulation and the measurement have similar behaviours. Table 23 presents the differences between the simulation and measurement.

Table 23. "Large 1" pair analysis of simulation and measurement differences at 3 W.

Step	Losses in Simulation (W)	Losses in Measurements (W)	Flat Difference (mW)	Absolute Difference (%)	Step Yield Simulated (%)	Step Yield Measured (%)	Percentage Points Difference	Relative Yield Difference (%)
A	3.28	3.28	0	0.00	X	X	X	X
B	3.18	3.18	0	0.00	96.95	96.95	0.00	0.00
C	3.00	3.00	0	0.00	94.34	94.34	0.00	0.00
D	2.81	2.81	0	0.00	93.67	93.67	0.00	0.00
E	2.50	2.50	0	0.00	88.97	88.97	0.00	0.00
F	2.40	2.40	0	0.00	96.00	96.00	0.00	0.00
G	1.61	1.55	60	3.73	67.08	64.58	2.50	3.73
H	1.54	1.54	0	0.00	95.65	99.35	3.70	3.87
I	1.37	1.37	0	0.00	88.96	88.96	0.00	0.00
End-to-end efficiency (%)	41.77%	41.77%	X	0.00%	41.77%	41.77%	X	X

Table 23 validates that the simulation and measurement are almost the same. Furthermore, solving the supply power reduces the difference between the simulation and measurements. The coupling Step "F" still has a high difference; adding a tuning capacitance to the receiver antenna would reduce these inconstancies. The simulation is again in tune with the criterion of 5% difference regarding the end-to-end efficiencies.

This validates the proper accuracy of the simulation, independently of the antenna pair.

The difference between Figures 14–16 is due to changes in chip configuration. Figures 15 and 16 are designed to allow for more communication and not just charging. This requires the chip to have higher sensitivity and thus means that it consumes more power in the form of chip losses. Also, the power supply is the same for the simulations and measurements.

Table 24 presents all simulated and measured coupling coefficients, as well as the simulated and measured end-to-end efficiency at 2 W and 3 W.

Table 24. Coupling coefficient modelled and measured and end-to-end efficiency depending on supply power for all antennas pairs. Note: values in **bold** refer to different configurations than other values in the table.

Antenna Pair	Modelled Coupling Coefficient	Measured Coupling Coefficient	2 W Efficiency Simulated	3 W Efficiency Simulated	3 W Efficiency Measured	3 W Gap
Small 1	0.57	0.58	59.7%	55.56%	58.30%	2.74
Small 2	0.49	0.48	64.2%	**56.40%**	**57.01%**	0.61
Small 3	0.45	0.45	61.2%	58.40%	X	X
Large 1	0.47	0.47	52.4%	**41.77%**	**41.77%**	0.00
Large 2	0.56	0.56	59.1%	56.00%	X	X
Large 3	0.61	0.60	62.9%	60.40%	X	X
Planar	X	0.39	38.0%	41.40%	X	X

The pairs were measured at 3 W, because all simulations displayed the same evolutions. With the same configuration, 3 W is the maximal power output, therefore representing the key point of the comparison.

4. Discussion

Modelling of the antennas and coupling coefficient has been validated with VNA measurements of the fabricated antennas. The simulation respects the quality criteria of a maximum absolute difference of 5 percentage points between the simulated and measured values for different pair configurations and applications. The validation of this point justifies using the simulation as a viable way to compare antenna pairs. The simulation at 2 W shows better end-to-end efficiencies due to the reduction in the voltage crossing the components, thus reducing the Joule's effect. All prototype antenna pairs show better coupling factors than the reference, with a reduction in the losses among the antennas and a reduction in the losses due to the coupling coefficient. In compact wireless power transfer, misalignment and positioning tolerances heavily impact the coupling coefficient and system efficiency, as characterized for multi-coil arrays by [37], and further parameterized for misalignment conditions by [38]. In this work, the issue has been avoided by using the support presented in Figure 2a.

The antenna pair "Small 2" is composed of a small emitter and medium receiver. It is one of the configurations displaying the highest efficiency for end-to-end power transfer among the investigated prototype pairs. At 2 W, it reaches the best simulated efficiency, as shown in Table 24, of 64.2%, slightly above the other configurations. At 3 W, however, the behaviour becomes more balanced: "Small 1" and "Small 2" exhibit very close efficiencies, with "Small 1" ranking slightly above "Small 2" in the simulation according to Table 24. Despite not always being the configuration with the highest coupling coefficient "k", the values of the antennas' characteristics propose a good balance between coupling coefficient and antenna characteristics to minimize the energy dissipated through Joule's effect. The measurements of the "Large 1" and "Small 2" pairs validate the efficiency estimation of the simulation, even for different applications of the same pairs.

Regarding future work, adding ferrite rods consistently improves the coupling coefficient of the prototype pairs, as does the ferrite sheet addition for the reference antennas. The impact of the other ferrite shapes and the combination of ferrites could facilitate the phenomenon of a difference between the coupling coefficient and end-to-end efficiency. One condition is to check the impact of the ferrites on the antennas' characteristics. The impact of the power emitted should also be studied to verify if the ferrite shows a variation in temperature that could lead to a shift in the permeability of the ferrite, impacting the coupling coefficient and the equivalent characteristics of the antennas and the power dissipated in it. of the addition of ferrite should be studied, depending on the ferrite material, and the usage of different rod diameters could be effective for larger antenna radii.

A second perspective would be to study the impact of a diode bridge on the antenna's impedance and coupling coefficient, allowing us to extract an equation to predict the coupling coefficient shift and to track more precisely the power available at each antenna and lost in the coupling. An alternative could be the development of a measurement methodology to improve the accuracy of the S2P measurement, allowing for better extraction in the same environment compared to the power transfer measurement. A last alternative to pursue in the development of this antenna's 3D form factor is to verify the ability of the antenna to perform NFC communication and observe the impact of the communication steps on the efficiencies shown in this study for wireless charging applications.

5. Conclusions

This work proposed and evaluated a concentric 3D helicoidal antenna architecture for NFC wireless charging dedicated to smart ring applications. The analytical models used to estimate the antenna's electrical characteristics and coupling coefficients were first validated against VNA measurements of the fabricated prototypes. The measured antenna parameters and coupling coefficients showed good agreement with the calculated values, supporting the use of the proposed modelling approach for the investigated geometries.

An end-to-end power transfer model was then developed using the measured S-parameters of the antenna pairs. The comparison between simulated and measured power budgets demonstrated that the simulation reproduces the experimental behaviour within the criterion of a 5 percentage point absolute difference in end-to-end efficiency defined in this study. In particular, the measurements presented in Figures 15 and 16 confirm the simulated power transfer behaviour for the "Small 2" and "Large 1" pairs at 3 W.

The experimental validation performed with the antenna pairs ("Small 1", "Small 2" and "Large 1"), under different operating configurations, supports the applicability of the simulation framework to the range of prototype geometries investigated in this work. On this basis, the realised 3D prototype pairs show higher simulated end-to-end power transfer efficiency than the reference planar antenna pair.

At 2 W, the prototype simulations achieve an average end-to-end efficiency of approximately 60%, compared with 38% for the reference configuration, corresponding to an average absolute gain of 22 percentage points. The best performing configuration at 2 W is "Small 2", reaching 64.2% efficiency in simulation. At 3 W, the prototypes achieve an average efficiency of approximately 57%, compared with 41% for the representative planar reference, corresponding to an average absolute gain of 16 percentage points. At this power level, the efficiencies are more balanced between configurations: "Small 1" slightly outperforms "Small 2" in simulation according to Table 24, while both remain above the reference configuration. These results demonstrate that the highest coupling coefficient does not necessarily lead to the highest end-to-end efficiency. Although the best coupling values are not always associated with the best power transfer performance, the overall balance between magnetic coupling, antenna resistance, quality factor, and Joule's effect losses remains decisive. The proposed 3D helicoidal architecture therefore provides a suitable compromise between geometrical integration, coupling, and electrical losses for compact ring-shaped NFC wireless charging applications.

Future work aims to investigate the influence of ferrite geometry and material, antenna behaviour under realistic non-linear receiver loading, and the simultaneous use of the proposed antenna architecture for complete NFC and wireless charging applications.

Author Contributions: Conceptualization, L.R., T.D., A.L. and J.Q.; methodology, L.R., T.D., A.L. and J.Q.; software, L.R., J.Q.; validation, L.R., T.D., A.L. and J.Q.; formal analysis, L.R., T.D., A.L. and J.Q.; investigation, L.R.; resources, L.R., T.D., A.L. and J.Q.; data curation, L.R.; writing—original draft preparation, L.R.; writing—review and editing, L.R., T.D., A.L. and J.Q.; visualization, L.R., T.D., A.L. and J.Q.; supervision, L.R., T.D., A.L. and J.Q.; project administration, T.D., A.L. and J.Q. All authors have read and agreed to the published version of the manuscript.

Funding: This research was funded by Aix Marseille Univ, Univ Toulon, CNRS, ISEN-Yncréa Méditerranée, IM2NP grant number 2024/00669. The funding was provided in the context of a CIFRE PhD Thesis of Lilian Rolle.

Data Availability Statement: The original contributions presented in this study are included in the article. Further inquiries can be directed to the corresponding author.

Conflicts of Interest: Authors Lilian Rolle and Jérémy Quignon were employed by the company STMicroelectronics. The remaining authors declare that the research was conducted in the absence of any commercial or financial relationships that could be construed as a potential conflict of interest.

Abbreviations

The following abbreviations are used in this manuscript:

NFC	Near-field communication
IoT	Internet of things
NFC WLC	Near-field communication wireless charging
BOM	Bill of materials
ADS	Advanced design system
VNA	Vector Network Analyzer
LDO	Low drop-out
RFO	Chip output driver
EMI	Electromagnetic interference
RFI	Chip input driver
PETG	Polyethylene terephthalate glycol
PLA	Polylactic acid
DC	Direct current
RMS	Root mean square

References

1. Samsung. Available online: https://www.samsung.com/us/rings/galaxy-ring/ (accessed on 7 April 2026).
2. Grand View Research. Available online: https://www.grandviewresearch.com/industry-analysis/smart-rings-market-report (accessed on 7 April 2026).
3. Huang, Q.; Ma, Z.; Wang, S.; Yang, Y. Integration of Near-Field Communication (NFC) Antenna and Wireless Charging Coil for Portable Electronic Products. *IEEE J. Emerg. Sel. Top. Power Electron.* **2024**, *12*, 3415–3425. [CrossRef]
4. Fischbacher, R.; Lopera, J.R.; Pommerenke, D.; Prestros, R.; Auinger, B.; Bösch, W.; Grosinger, J. WPT and NFC Interoperability for Wearables with Miniaturized Coils. In *Proceedings of the 2023 IEEE 13th International Conference on RFID Technology and Applications (RFID-TA), Aveiro, Portugal, 4–6 September 2023*; IEEE: Piscataway, NJ, USA, 2023; pp. 33–36.
5. Dentis, A.; Cantore, L.; Concadoro, S.; Demarchi, D.; Ros, P.M. A 13.56 MHz Inductive Wireless Power Transfer System for Active Implantable Medical Devices. In *Proceedings of the 2025 32nd IEEE International Conference on Electronics, Circuits and Systems (ICECS), Marrakech, Morocco, 17–19 November 2025*; IEEE: Piscataway, NJ, USA, 2025; pp. 1–4. [CrossRef]
6. Biswas, D.K.; Sinclair, M.; Hyde, J.; Mahbub, I. An NFC near-field communication based wireless power transfer system design with miniaturized receiver coil for optogenetic implants. In *Proceedings of the 2018 IEEE Wireless Power Transfer Conference (WPTC), Montreal, Quebec, Canada, 3–7 June 2018*; IEEE: New York, NY, USA, 2018; pp. 1–4.
7. Quignon, J.; Tornambe, A.; Deleruyelle, T.; Pannier, P. Antenna System Design to Increase Power Transfer Efficiency with NFC Wireless Charging Technology. *Adv. Sci. Technol. Eng. Syst. J.* **2022**, *7*, 123–128. [CrossRef]
8. iFixit. Available online: https://www.ifixit.com/News/98423/samsungs-galaxy-ring-revealed (accessed on 12 May 2026).
9. Voyager.lumafield. Available online: https://voyager.lumafield.com/project/fc34d58b-2716-4276-af65-066b9e1224e3 (accessed on 12 May 2026).

10. Beckystern. Available online: https://beckystern.com/2024/06/26/ultrahuman-ring-air-teardown/ (accessed on 12 May 2026).
11. Tahseen, H.U.; De Pascali, C.; Esposito, V.; Colella, R.; Catarinucci, L.; Francioso, L. Enhanced Range Dual-Coil NFC Antenna System for Diverse Near Field Applications. In *2025 10th International Conference on Smart and Sustainable Technologies (SpliTech), Bol and Split, Croatia, 16–20 June 2025*; IEEE: Piscataway, NJ, USA, 2025; pp. 1–5.
12. Nguyen, S.; Duong, C.; Amirtharajah, R. A Smart Health Tracking Ring Powered by Wireless Power Transfer. In *Proceedings of the 2021 IEEE Wireless Power Transfer Conference (WPTC), San Diego, CA, USA, 1–4 June 2021*; IEEE: Piscataway, NJ, USA, 2021; pp. 1–4.
13. Antique Jewellery Company. Available online: https://www.antiquejewellerycompany.com/average-ring-sizes-for-men-and-women/ (accessed on 12 May 2026).
14. Loopsens. Available online: https://www.loopsens.com/produit/movano-evie-ring/ (accessed on 12 May 2026).
15. Amazfit. Available online: https://fr.amazfit.com/products/amazfit-helio-ring (accessed on 12 May 2026).
16. Lunazone. Available online: https://www.lunazone.com/products/luna-smart-ring-gen-2?srsltid=AfmBOorCnArO-D_OpKzIMKsBU0bsAm47AWQu8CFvfpee2xRkim3jgOUh (accessed on 12 May 2026).
17. Sokai. Available online: https://soxai.co.jp/?srsltid=AfmBOooeRU4NMiq1pH4zvSWwF8uYalEvUeYWfNIm6j_RdUUiFjpm-6v7 (accessed on 12 May 2026).
18. VeliaRing. Available online: https://veliaring.com/pages/ring-tech-specs?srsltid=AfmBOoppEZ_GnbYFuWkJ6uITPkhGbEx4FjoniGlv54h0_b-vqBVcR9xb (accessed on 12 May 2026).
19. Ouraring. Available online: https://support.ouraring.com/hc/fr/articles/33045011508115-Oura-Ring-4 (accessed on 12 May 2026).
20. Circular. Available online: https://shop.circular.xyz/products/circular-ring-2?_gl=1*4mgmq0*_gcl_au*MTc3ODg4ODczNy4xNzg3MzA0NzAz&variant=54761919545689 (accessed on 12 May 2026).
21. RingConn. Available online: https://ringconn.com/fr/products/ringconn-gen-3?variant=49061926797620 (accessed on 12 May 2026).
22. Ultrahuman. Available online: https://www.ultrahuman.com/fr/ring/buy/?srsltid=AfmBOoqL3y4ko3StxfIu9xSfGmY-VmRty7VO1K-g4VzlIzNuWeGIbuRW (accessed on 12 May 2026).
23. Samsung. Available online: https://www.samsung.com/be_fr/rings/galaxy-ring/galaxy-ring-titanium-black-size-none-sm-q5kaph/ (accessed on 12 May 2026).
24. Zhu, X.; Xing, M.; Ye, J.; Liu, X.; Ren, Z. Design and optimization of a novel solenoid with high magnetic uniformity. *Sci. Rep.* **2024**, *14*, 24650. [CrossRef] [PubMed]
25. Rosa, E.B.; Grover, F.W. Formulas and Tables for the Calculation of Mutual and Self Inductance. (Revised.). *J. Wash. Acad. Sci.* **1911**, *1*, 14–16.
26. Wheeler, H.A. Simple Inductance Formulas for Radio Coils. In *Proceedings of the Institute of Radio Engineers, New York, NY, USA, 31 October 1928*; IEEE: New York, NY, USA, 1928; Volume 16, pp. 1398–1400.
27. Pérez-Nicoli, P.; Silveira, F.; Ghovanloo, M. *Inductive Links for Wireless Power Transfer*; Springer International Publishing: Cham, Switzerland, 2021; pp. 8–9.
28. Finkenzeller, K. *RFID Handbook: Fundamentals and Applications in Contactless Smart Cards and Identification*; John Wiley & Sons: Hoboken, NJ, USA, 2003. [CrossRef]
29. Buchmeier, G.G.; Takacs, A.; Dragomirescu, D.; Ramos, J.A.; Fortes Montilla, A. Optimized Rectangular Planar Coil Design for Wireless Power Transfer with Free-Positioning. In *Proceedings of the 2021 IEEE Wireless Power Transfer Conference (WPTC), San Diego, CA, USA, 01–04 June 2021*; IEEE: Piscataway, NJ, USA, 2021; pp. 1–6.
30. Grover, F.W. *Inductance Calculations: Working Formulas and Tables*; Van Nostrand: New York, NY, USA, 1981.
31. Conway, J.T. Inductance Calculations for Noncoaxial Coils Using Bessel Functions. *IEEE Trans. Magn.* **2007**, *43*, 1023–1034. [CrossRef]
32. Bouklachi, M.; Biancheri-Astier, M.; Diet, A.; Le Bihan, Y. Energy harvesting of a NFC flexible patch for medical applications. In *Proceedings of the 2019 IEEE Wireless Power Transfer Conference (WPTC), London, UK, 18–21 June 2019*; IEEE: Piscataway, NJ, USA, 2019; pp. 1–5.
33. Iqbal, M.A.; Raza, S.; Javed, A. Ferrite Incorporated Wireless Power Transfer Efficiency Improvement Systems. In *Proceedings of the 2020 IEEE International Conference on Robotics, Automation and Artificial Intelligence (RAAI), Sukkur, Pakistan, 29–30 January 2020*; IEEE: New York, NY, USA, 2020; pp. 1–8.
34. Dong, Z.; Xu, Q.; Tu, J.; Zhu, Y.; Li, J.; Hu, Y.; Ren, H.; Dong, P.; Xue, Z.; Cheng, X. A Dual-Layer Reverse-Helical Inductive Wireless Passive Flexible Temperature Sensor Integrated with Ferrite for Bearings Monitoring. *IEEE Sens. J.* **2025**, *25*, 37276–37287. [CrossRef]
35. Divide by Zero. Available online: https://www.divbyz.com/knowledge-center/materials/petg (accessed on 9 February 2026).
36. Zhang, S.; Njoku, C.; Whittow, W.; Vardaxoglou, J.Y. Novel 3D printed synthetic dielectric substrates. *Microw. Opt. Technol. Lett.* **2015**, *57*, 2344–2346. [CrossRef]

37. Zhao, W.; Mai, S. Design of High Efficiency Planar Spiral Coil for Implantable Wireless Power Transfer Systems. In *Proceedings of the 2022 IEEE International Symposium on Circuits and Systems (ISCAS), Austin, TX, USA, 27 May–1 June 2022*; IEEE: Piscataway, NJ, USA, 2022; pp. 147–151.
38. Lan, L.; Arteaga, J.M.; Pucci, N.; Mitcheson, P.; Yeatman, E.; Young, D.; Roundy, S. Misalignment Parameterization of a 13.56 MHz Inductive Power Transfer System for in-situ Soil Sensing. In *Proceedings of the 2022 IEEE Wireless Power Week (WPW), Salt Lake City, UT, USA, 12–15 December 2022*; IEEE: Piscataway, NJ, USA, 2022; pp. 1–4.

Disclaimer/Publisher's Note: The statements, opinions and data contained in all publications are solely those of the individual author(s) and contributor(s) and not of MDPI and/or the editor(s). MDPI and/or the editor(s) disclaim responsibility for any injury to people or property resulting from any ideas, methods, instructions or products referred to in the content.